

Chapter 3

Advances in Optoacoustic Imaging: From Benchside to Clinic

Chris Jun Hui Ho, Neal C. Burton, Stefan Morscher, U. S. Dinish, Josefine Reber, Vasilis Ntziachristos and Malini Olivo

Abstract Optoacoustic imaging has been widely used for in vivo disease diagnosis and therapy monitoring. Acquisition hardware, analysis, and contrast agents have been subject to much innovation, creating access to an ever-growing range of biomedical applications. In this review, a broad overview of optoacoustic theory, instrumentation and data processing is provided, together with the various categories of contrast agents that have been developed. In addition, the application of these techniques and contrast agents in preclinical and clinical imaging applications will be discussed in detail, ranging from imaging of cancer and various organs like skin, brain and breast to sentinel lymph node mapping. Finally under conclusions, we highlighted future perspectives in this field, in the context of instrumentation and software development, as well as advances in clinical translation.

C.J.H. Ho · U. S. Dinish · M. Olivo
Bio-Optical Imaging Group, Singapore Bioimaging Consortium, Agency for Science,
Technology and Research, Singapore, Singapore
e-mail: chris_ho@sbic.a-star.edu.sg

N.C. Burton · S. Morscher · J. Reber · V. Ntziachristos
Helmholtz Center Munich, Institute for Biological and Medical Imaging, Neuherberg,
Germany

N.C. Burton · S. Morscher
Ithera Medical, GmbH, Munich, Germany

S. Morscher · J. Reber · V. Ntziachristos
Technical University of Munich, Munich, Germany

M. Olivo (✉)
School of Physics, National University of Ireland, Galway, Ireland
e-mail: malini_olivo@sbic.a-star.edu.sg

1 Introduction to Optoacoustics

1.1 Theory

With the photoacoustic (PA) effect being discovered as early as 1880 [1] by Arthur Graham Bell, its use for imaging applications has only been exploited in the past two decades. Whereas the initial setup audible signals were created by light pulses from a chopped beam of sunlight subsequently absorbed by sheet metal, Bell [2] later used infrared and ultraviolet light for spectroscopic applications.

In imaging, this methodology can be used to overcome light scattering in biological tissues where light pulses are diffusive and exponentially decaying beyond the first millimeter, after the ballistic regime. In particular, acoustic detection in photoacoustic imaging (PAI) can provide imaging of deep tissues up to a few centimeters based on light absorption, not only in the near-infrared (NIR) optical window, but also in the visible and infrared ranges [3, 4]. Myriad applications exist for imaging endogenous tissue chromophores such as hemoglobin and melanin, or exogenous contrast agents such as fluorophores, nanoparticles and genetically engineered proteins (Fig. 1). Extending this rich toolset even further, thermoacoustic imaging by use of electromagnetic waves as an excitation source has enabled imaging using more diverse contrast [5].

Where raster scanning approaches dominate for photoacoustic microscopy (PAM) [6] and also have been recently used for high-resolution mesoscopy [7], imaging using linear and tomographic ultrasound arrays remains the preference for most deep tissue applications in preclinical and clinical environments [8]. Multispectral Optoacoustic Tomography (MSOT) [9] is a specific implementation using tomographic detection approaches in combination with multispectral excitation to separate specific contributions from individual tissue chromophores, hence increasing specificity. While other commercially available implementations exist [10–12], this section will focus on the MSOT family with its requirements, implementation and applications.

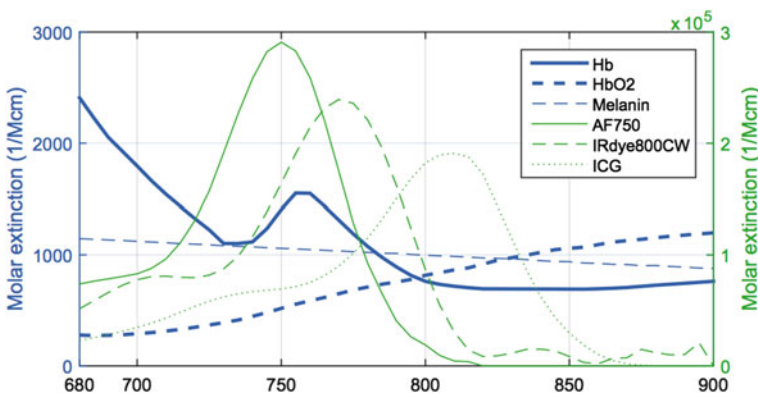


Fig. 1 Absorption spectra of typical endogenous and exogenous chromophores

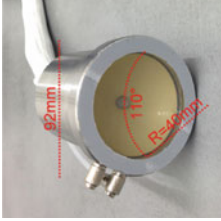
1.2 Instrumentation

A decisive factor determining the success of PAI in general and MSOT imaging specifically is a combination of hardware components with defined parameters. Most importantly, a light source is required in order to produce nanosecond light pulses in the NIR. Typically for a laser with a repetition rate of 10 Hz, pulse energies of more than 20 mJ are beneficial for most applications in order to stay close to the American National Standards Institute (ANSI) dictated maximum permissible exposure (MPE) of 20 mJ/cm² for use in humans, while at the same time providing homogeneous surface illumination to maximize delivered energy. Another important aspect is the seamless, wideband tuning capability of the laser that opens up various applications, where wavelengths in the NIR range (680–980 nm) attainable by a neodymium-doped yttrium aluminium garnet (Nd:YAG) pumped optical parametric oscillator (OPO) are applicable for many relevant applications. Only imaging of lipids as discussed in later sections demands higher wavelengths. The wavelength switching speed is important for multispectral excitation, since it determines the effective multispectral imaging rate. Higher repetition rates are beneficial as they reduce the impact of motion in between wavelengths especially when employed in handheld mode, but they also reduce both the available per-pulse energies as well as the MPE. The laser employed for MSOT is specifically designed to meet its demands and deliver peak energies >100 mJ at 10 Hz, or >30 mJ at up to 50 Hz with wavelength tuning between pulses (in less than 20 ms) with a range from 660 to 2300 nm, depending on the laser model.

Emitted acoustic waves have to be detected by an ultrasound detector that converts them into voltage values. While more sophisticated and broadband optical detectors are being developed presently [13], conventional piezo-composite based detectors still dominate the field for their superior sensitivity and robustness. Grouping the detectors in arrays allows reconstruction of a complete image with all projections acquired in a single laser pulse and allows real-time feedback of the imaged sample. This is one of the key requirements for handheld operation. Detector arrays employed by MSOT to this point include cylindrically focused arc-type 2D detectors, as well as spherical 3D arrays, as shown in Table 1. While the radial resolution is largely determined by the bandwidth of the transducer, the transversal resolution depends on the overall transducer arrangement and size.

Electrical signals, created by the transducer, must be digitized and transferred to an attached computer for reconstruction and storage. A digital range of 12 bits and a sensitivity in the low μV have been adopted as a standard in the field, where sampling a sufficient number of transducer channels simultaneously at a sampling rate well within the Nyquist-Shannon criterion is one of the more challenging aspects. MSOT custom electronics use 12 bits and 4 $\mu\text{V}/\text{LSB}$ and samples up to 512 channels at the same time at a sampling rate of 40 mega-samples/s, allowing detection of signals up to 20 MHz. An additional, first order Butterworth low pass filter with a cut-off of approximately 13 MHz helps to avoid possible aliasing in hardware. In some systems on the market, transmit electronics for active ultrasound

Table 1 Example detectors used in MSOT implementations

	inVision	2D handheld	3D handheld
			
Center frequency	5.0 MHz	4.0 MHz	2.5 MHz
Bandwidth	60 %	50 %	60 %
Radial resolution	~ 150 μm	~ 190 μm	~ 300 μm
Number of elements	128/256/512	256	384
Angular coverage	270°	135°	110°
Radius	40 mm	40 mm	40 mm
Field of view	30 \times 30 mm	25 \times 25 mm	20 \times 20 \times 25 mm

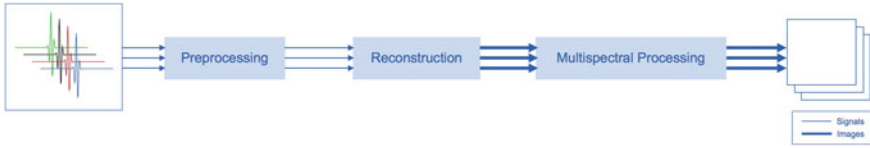


Fig. 2 Flowchart of typical processing tasks for MSOT imaging

imaging are integrated into the receive electronics to enable interleaved ultrasound imaging, where the challenge lies in sustaining high detection sensitivities in the μV range for PAI while at the same time creating excitation pulses that can exceed 80 V peak-to-peak voltage on the same signal train.

1.3 Data Processing

Once digitized, a number of preprocessing tasks need to be executed prior to the actual image reconstruction and subsequent multispectral processing, as shown in Fig. 2. While many of the operations are usually quite straightforward, they do play an important role in the resulting MSOT image and its meaning regarding quantification, so care is to be taken when deciding the parameters. Many of the aforementioned tasks can easily be performed in hardware such as digital signal processors (DSPs), but can also be executed with software, preferably on a graphical processing unit (GPU), as is the case for the presented MSOT implementation.

With signals digitized and transferred to the computer, they are still subject to a direct current (DC) offset and low frequency artifacts. As a simple rule of thumb, the lower passband edge frequency can be estimated using $f_{PB} = \frac{c}{d}$ with c being the speed of sound (~ 1530 m/s in tissue) and d the diameter of the region of interest, assuming that low frequency variations in the scale of the field-of-view (FOV) are negligible. For a FOV of 30×30 mm, this means that a low cut-off around 50 kHz can be used for typical MSOT implementations. In terms of filter design, the transition band should be narrow enough to sufficiently cancel parasitic low frequencies, but not too narrow to omit strong ripples in the filtering process: 10 kHz (80 % of the edge frequency) proved to be well-suited for the presented case. In order to avoid phase perturbations, the use of high-order finite impulse response (FIR) filters with linear phase relation is recommended.

As another important measure, the electrical impulse response (EIR) of the transducer should be corrected, in order to enable accurate reconstruction throughout the frequency band of the transducer. The impulse response can be obtained via measurement or using the transducer specifications. A measurement can be performed by imaging a sub-resolution target (e.g. a small microsphere) in the center of the transducer, and this measurement can be used to deconvolve the acquired signals for other specimens. The upper -3 dB edge frequency of the

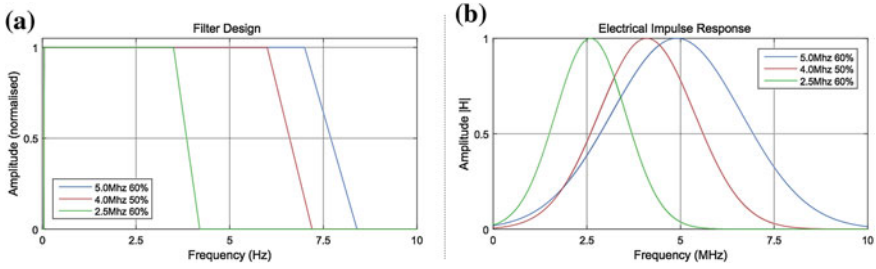


Fig. 3 Suggested filter design (a) and EIR (b) of example detectors

transducer is a good default for the upper passband edge frequency of the filter, in order to prevent high frequency noise amplification in the process of deconvolution. In addition, it is convenient to perform both filtering and deconvolution in the frequency domain, where filtering turns into a mere multiplication and deconvolution is simplified to a division. Examples for filter design and the amplitude of electrical impulse responses for the given transducer examples are shown in Fig. 3.

A number of approaches exist to produce tomographic images from the acquired optoacoustic signals [14]. Simple approaches only consider a backprojection of signals based on time-of-flight, where more sophisticated model-based approaches [15] enable more complex modelling of different aspects of the signal propagation.

Backprojection attributes all signals captured by an individual transducer at a certain point in time to all possible source locations (pixels), which are identified by their distance to the sensor element and hence lie on an arc. The advantages of the simple concept are low computational demand and a high degree of independence among the individual operations, allowing fast parallel execution on a GPU.

Model-based reconstruction calculates a geometric model that incorporates the detection geometry and a variety of other parameters, including the variable speed of sound, detector shape [16], EIR and distribution of acoustic scatterers. Once the model is created, it is inverted and multiplied with the acquired signals. Iterative inversion using a least squares approach is the simplest approach, but usually takes a few seconds per image so does not fulfill the requirements for live image display. Use of wavelet packets [17] for the inversion provides a significant acceleration and also allows band-separated post-processing, in order to correct for frequency-dependent variations in local sensitivity based on the reconstruction geometry.

Both methods ultimately result in a map representing the acoustic source distribution in the imaging grid. Most applications, however, require an absorption map that can be retrieved from the pressure map by incorporating the light fluence distribution. Modelling light flux in the sample is a complex process and requires knowledge of the optical properties (absorption and scattering coefficients), where only absorption can be obtained from the optoacoustic measurement. Furthermore, even in cases where the reconstruction problem is simplified to a 2D problem based on the utilized detection geometry, the light fluence distribution problem remains 3D. With Monte-Carlo methods being the gold standard for light fluence calculation

[18], a number of approaches have been presented to solve the problem individually or using a model based approach [19].

Multispectral illumination is the essential feature which brings MSOT applications beyond simple anatomical imaging, by enabling the resolution of individual intrinsic and extrinsic chromophores based on their distinct absorption spectra, hence providing both functional and molecular contrast. This enables not only the separation of contributions of oxy- and de-oxygenated hemoglobin to the intrinsic background signal and thus the determination of oxygen saturation in tissue, but also the analysis of biodistribution of melanin or injected contrast agents.

As a general rule of thumb, at least 5 wavelengths are recommended for multispectral imaging, where up to 15 can provide improved results in cases where multiple chromophores need to be resolved from the background. The choice of wavelengths should always include peak absorption wavelengths of chromophores and other decisive points. In *in vivo* settings, a basic set including 700, 730, 760, 800 and 850 nm proved reliable to enable good separation from the background. All described methods result in distribution maps of individual absorbers that are usually overlaid using a gradual alpha map onto an anatomical background image, usually taken at 800 nm, which is the isosbestic point of hemoglobin.

One of the most widely used and most reliable methods is spectral fitting of known absorption spectra (S) to the measured spectral profiles using the Moore-Penrose pseudoinverse. It requires a priori knowledge about the chromophores expected in the sample and their absorption spectra (S) to unmix the individual absorbers (U) from the mixed data obtained by the measurement (M).

$$M = SU$$

$$U = S^{-1}M$$

Another route involves the utilization of statistical properties in the process of unmixing. Independent component analysis (ICA) [20] tries to maximize statistical independence in the wavelength dimension of the measurement data. It can optionally be provided with a priori spectra of expected absorbers to guide the optimization process (Guided ICA). Apart from the statistical optimization, the key difference to spectral fitting as described above is the operation in mean-free space. This approach can also be used to generate an optimized unmixing matrix on a known positive dataset, which in turn is used to provide comparable results for all datasets in a study [21]. A third approach involves theory from signal processing, where an adaptive matched filter (AMF) is created from the absorption spectra of expected chromophores [22]. It works by trying to reveal the desired absorber contributions using a previously generated background model. Conceptually, the method will not work for dominant background absorbers, but is merely optimized for revealing extrinsically administered agents with a background model created on a dataset in absence of the absorber of interest.

2 Optoacoustic Contrast Agents

Up to date, a great variety of PA contrast agents have been developed, which include fluorescent dyes, metal nanoparticles (gold/silver), carbon-based materials (carbon nanotubes, graphene), gene reporters, “smart” activatable probes and many others. However, out of all these, there is no single contrast agent which is suitable for all applications. When choosing a contrast agent for a specific application, one needs to consider many factors, which include the absorption spectrum, size and shape, chemical composition and surface chemistry, targeting ligands, and in vivo stability and toxicity. For instance, contrast agents can be bioconjugated with specific targeting moieties to cater to various applications ranging from tumor detection, sentinel lymph node mapping, oxygenation and angiogenesis monitoring to the characterization of atherosclerotic plaques and monitoring of therapeutic treatment. Multifunctional, multimodal contrast agents have also been developed, which can offer imaging and therapy in a single construct, or simultaneously provide contrast in multiple imaging modalities. In this section, various categories of PA contrast agents will be discussed in greater detail: fluorophores which have been used in clinical trials and thus, nearer towards clinical translation as PA contrast agents compared to others, genetic reporters, activatable contrast agents, as well as upcoming novel classes of PA contrast agents such as polymers, metal carbonyls and upconversion nanoparticles, which offer potential to be further developed for specific applications.

2.1 Fluorophores

Many fluorophores such as dyes, proteins, photosensitizers—which have been widely used in pure optical imaging—can be potential PA contrast agents. Out of these fluorophores, some photosensitizers and the FDA-approved dye, indocyanine green (ICG), which have been widely used in clinical trials, will be covered in this section.

There are many known advantages of photosensitizers, which include preferential tumor uptake, PDT efficacy, as well as clinical relevance, offering them great potential as theranostic contrast agents. However, many of these photosensitizers have been reported to exhibit low fluorescence quantum yields [23], limiting their efficacy in fluorescence imaging. Yet, this limitation becomes an advantage for PAI, since weak fluorophores with low fluorescence quantum yields are more likely to possess strong PA activity, as an excited system relaxes back to the ground state either through fluorescence or heat generation. Thus, in this pursuit, many research groups have evaluated various categories of photosensitizers as potential PA contrast agents, which include methylene blue [24–27], porphyrins [28, 29], squaraines [30], BODIPYs [31], phthalocyanines [32] and naphthalocyanines [33, 34].

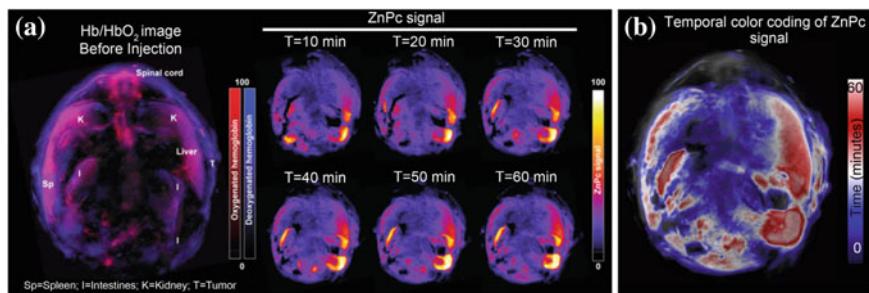
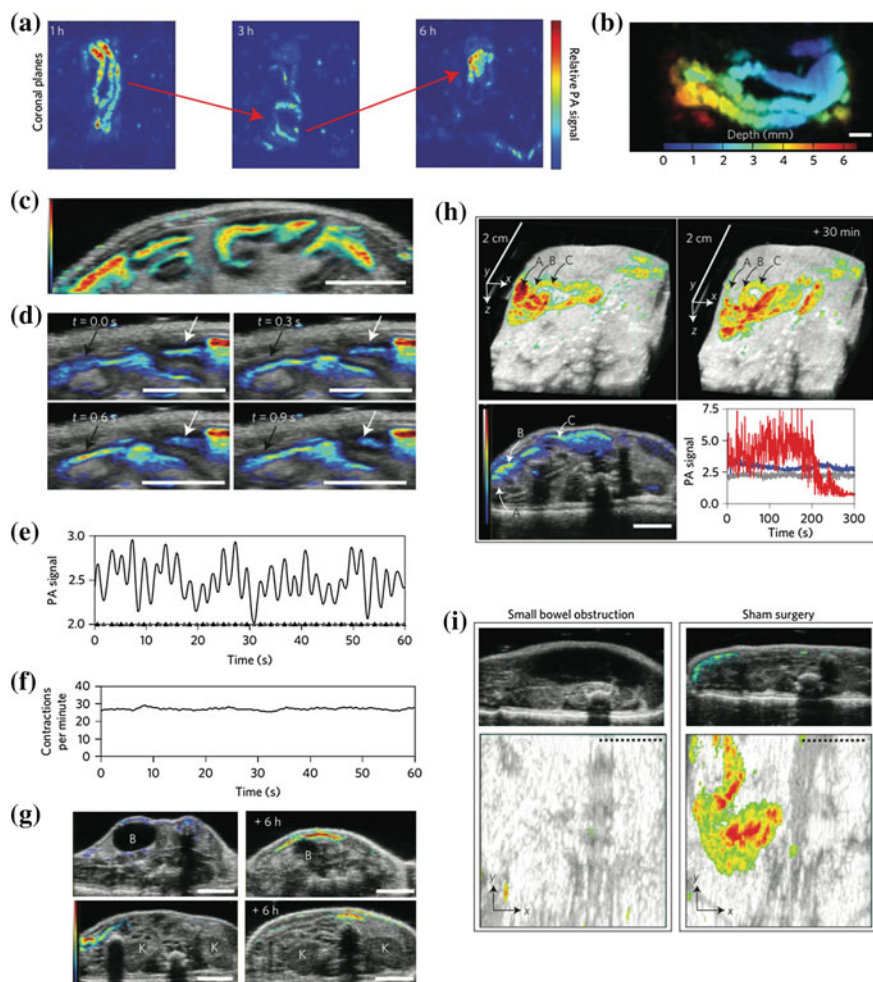


Fig. 4 a In vivo background-corrected MIP images of transverse slices through mouse pre-injection and within the first hour after injection, showing gradual probe accumulation within the tumor site and various organs over time. **b** Time-resolved color coding of the MSOT signal within the first hour after injection, demonstrating peak probe localization at the tumor site and various organs at 1 h post-injection. A stack of MIPs of ZnPc signal within the first hour post-injection is condensed in a parametric map visualizing the T_{\max} of ZnPc; peak concentrations of ZnPc are observed at $T = 60$ min. MIP—maximum intensity projection. (Reproduced with permission from [35])

In order to compare the efficacy of various photosensitizers as PA contrast agents, Olivo and team [35] examined the PA activity of 5 representative photosensitizers, zinc phthalocyanine (ZnPc), protoporphyrin IX (PpIX), 2,4-bis [4-(N, N-dibenzylamino)-2,6-dihydroxyphenyl] squaraine (Sq), chlorin e6 (Ce6) and methylene blue (MB) in phantoms, among which ZnPc exhibited the strongest PA signal. Then, they injected ZnPc intravenously into a mouse xenograft model and monitored its biodistribution and tumor localization using PAI. Results showed that this contrast agent accumulated at the tumor within 10 min post injection, reaching peak localization at 1 h (Fig. 4), with fast clearance within 24 h, thus, demonstrating the potential of photosensitizers as PAI contrast agents in vivo. They extended this study by examining the PA activity of 3 phthalocyanine photosensitizers, phthalocyanine tetrasulfonic acid (PcS4), Zn(II) phthalocyanine tetrasulfonic acid (ZnPcS4) and Al(III) phthalocyanine chloride tetrasulfonic acid (AlPcS4) [32]. Results showed that PcS4 offered the strongest PA activity both in phantoms and in tumor-bearing mice, with peak tumor localization at 1 h post-injection, making this time point ideal for photodynamic therapy treatment.

In addition, Lovell and coworkers [34] exploited the hydrophobicity of naphthalocyanine dyes to design ~20 nm frozen micelles, also called nanonaps which are stable and non-toxic in the gut, avoid systemic absorption and offer highly tunable optical NIR absorption for PAI. These nanonaps were used to image the gut anatomy, pathology and function in real-time at high resolution with low background (Fig. 5). In addition, they are also multimodal in nature, being imaged by ultrasound, positron emission tomography (PET) and PAI in a complementary manner.



◀ **Fig. 5** PAI of the intestine using nanonaps. **a** MIP of nanonaps following gavage of 100 ODs of ZnBNC nanonaps. *Red arrows* show nanonap transit. **b** Depth-encoded MIP of the intestine visualizing ZnBNC nanonaps. **c** Real-time multimodal mouse intestinal transverse plane with PA signal (*colour*) and simultaneous ultrasound (*grey*) acquisition following gavage of 100 ODs of ONc nanonaps. **d** Nanonap movement in the intestine. *Black arrow* shows inflow and *white arrow* shows outflow. **e** Intestinal ROI analysis. First-derivative zero crossings provide the time of maximal nanonap inflow (*black triangles*) and outflow (*grey triangles*) points. **f** Rate of contractile motion from the region, plotted over time. **g** Co-registered ultrasound for anatomical mapping of nanonaps. The bladder (B) and kidneys (K) are located with ultrasound (*grey*), and the nanonap PA signal is shown in colour. **h** ultrasound (*grey*)/PA (*colour*) MIPs of transverse slices, showing ONc nanonap intestinal transit over time. The MIP was used to orient the PA signal within a single slice of interest (*lower left*). Outflow quantification over time of nanonaps in area A (*red*) shown with reference to two others that maintained steady nanonap content in areas B (*blue*) and C (*grey*). The fluctuations in A are due to contractile inflow and outflow of nanonaps. **(i)** ultrasound/PA detection of intestinal obstruction. Mice were subjected to duodenal ligations or sham surgery. 100 ODs of ONc nanonaps were administered and mice were imaged 1 h later. The top images show a transverse slice 2.4 cm above the bladder, showing the swollen stomach in the obstructed mice. The *bottom images* show ultrasound/PA MIPs. An unobstructed flow of nanonaps is clear in the sham group. The *dashed line* indicates the approximate surgical incision site and the image width corresponds to 2.4 cm. OD—optical density; ZnBNC—zinc-2,11,20,29-tetra-tert-butyl-2,3-naphthalocyanine; ONc—5,9,14,18,23,27,32,36-octabutoxy-2,3-naphthalocyanine (ONc). (Reproduced with permission from [34])

On the other hand, Ntziachristos and team successfully employed contrast enhancement based on ICG to image its passive uptake in tumors [36] after systemic injection. In addition, they also made use of the clearance of ICG from the systemic circulation and its uptake in the liver and kidney [37, 38], to assess the functions of these organs. More recently, they also developed PEGylated liposomes incorporating ICG (LipoICG) as PA contrast agents [39], which in turn were able to resolve tissue localization with high sensitivity in tumor models over time. Non-invasive *in vivo* optical imaging was performed with detailed volumetric information through the entire tumor tissue showing the LipoICG distribution, as shown in Fig. 6. Other ICG conjugates developed for PAI include ICG-embedded nanoparticles [40] and ICG-conjugated single-wall carbon nanotubes [41].

2.2 Genetically Encoded Contrast Agents

Reporter genes are effective research instruments for tracking of cell migration, analysis of transfection efficiencies, as well as monitoring tumor growth rates. In recent years, reporters have also been exploited as an intrinsic optical absorption mechanism for PAI, especially in the field of gene expression. In general, an ideal reporter gene for deep tissue PAI should generate products that absorb light strongly in the NIR region, in order to produce strong PA signals.

In one of the pioneer studies, Wang and team [42, 43] demonstrated the use of the lacZ reporter gene in PAI of tumor activity. The lacZ gene encodes β -galactosidase, a bacterial enzyme responsible for lactose metabolism. In particular, they

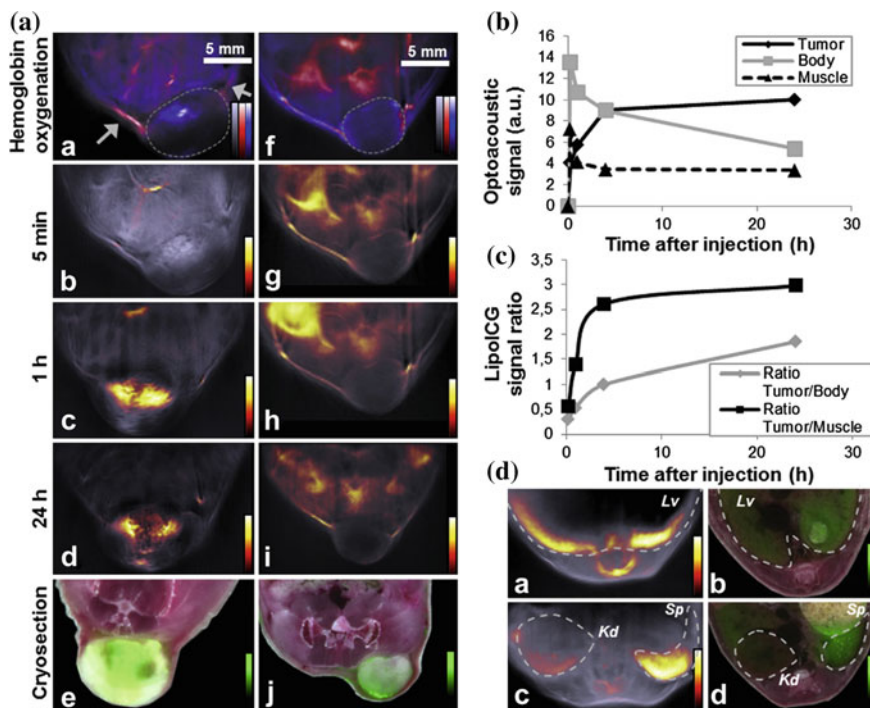


Fig. 6 Kinetics of LipoICG75 accumulation in 4T1 and HT29 tumor models imaged with MSOT. **a** Transverse MSOT image of a 4T1 tumor obtained using 800 nm illumination wavelength before injection of LipoICG75 (grey scale) overlaid with signal from oxy- (red) and de-oxygenated (blue) hemoglobin (arrows indicate the main blood vessels supplying the tumor) **a** Overlay of the MSOT LipoICG75 signal (hot scale) on a background image (grey scale) acquired at 800 nm illumination wavelength 5 min, 1 h and 24 h after injection (bed); Color image of a corresponding cryosection overlaid with the fluorescence signal from ICG (green scale). **e** Similar experiments performed on an HT29 tumor bearing mouse are depicted in the following column in the same arrangement **f-j**. **b** Maximum LipoICG75 signal intensity in the tumor (black line), the whole body without the tumor (grey line) and in the back muscles (dashed black line). **c** Maximum LipoICG75 signal intensity ratio between the tumor area and the whole body (grey line) and the back muscles (black line). **d** MSOT image of the liver (Lv) of a tumor-bearing animal acquired at 800 nm acquisition wavelength and overlaid with LipoICG75 signal (hot scale). **a** Fluorescent signal of the ICG channel (green scale) overlaid on the color picture of the cryosection in a comparable region of the liver. **b** Similar layout for the images of the same animal acquired at the kidney (Kd) and Spleen (Sp) region (ced). (Reproduced with permission from [39])

injected X-gal, a colorimetric assay for the lacZ-encoded enzyme β -galactosidase, into mice/rats and imaged lacZ-expressing tumors with high contrast using PAI. In addition, they also exploited various PAI setups for multi-scale imaging of lacZ expression, from macroscopic imaging of 5 cm thick biological tissue with a lateral resolution resolution of ~ 1.0 mm and an axial resolution of ~ 0.4 mm, to acoustic-resolution PAM imaging of a lacZ-expressing tumor and its surrounding vasculature with a lateral resolution of $45 \mu\text{m}$ and an axial resolution of $15 \mu\text{m}$, and

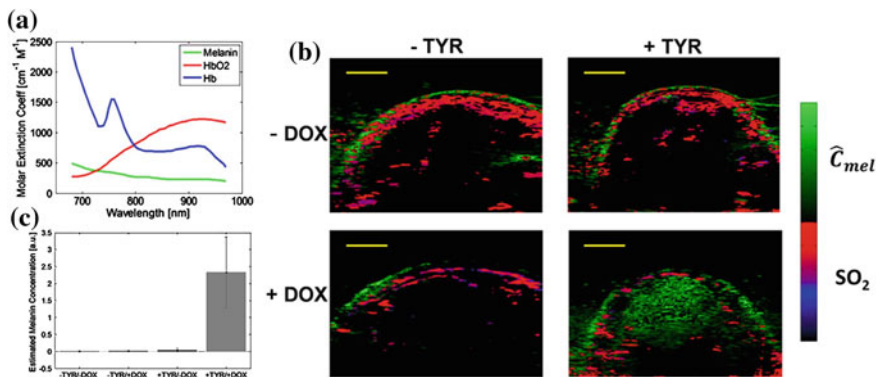


Fig. 7 **a** Molar extinction coefficient spectra of melanin, oxy-hemoglobin (HbO₂) and deoxy-hemoglobin (Hb). **b** Multispectral PAI of -TYR and +TYR tumors. The *green colormap* depicts melanin concentration while the *red-to-blue colormap* represents oxygen saturation. Scale bars correspond to 2 mm. **c** Quantification of relative melanin concentration levels. TYR—tyrosinase. (Reproduced with permission from [47])

to optical-resolution PAM imaging of intracellular localization of lacZ expression, with a lateral resolution of $<1 \mu\text{m}$. The need to inject a substrate locally provided a key limitation to this particular approach. Alternatively, they also used tyrosinase as a reporter gene for optical-resolution PAM imaging of tyrosinase-catalyzed melanin production in transfected cells [44]. Tyrosinase is the key enzyme regulating the production of melanin, which has a strong optical absorption. In addition, it possesses an enzymatic amplification mechanism, in which each expressed tyrosinase molecule can bring about the production of multiple melanin molecules, providing an amplified PA signal. These results demonstrated that PAI can be used to visualize gene expression in biological studies at both microscopic and macroscopic resolutions.

Similarly, Zemp and coworkers [45, 46] also used tyrosinase as a dual reporter gene for magnetic resonance (MR) and PAI. When tyrosinase-expressing MCF-7 cells were incubated with ferric citrate, they exhibited a T1 reduction in MR imaging and higher contrast in PAI, as compared to normal MCF-7 cells. In another study [47], tetracycline-inducible melanin expression in tyrosinase-tagged tumors is activated via doxycycline treatment, in contrast to low melanin expression in tumors before doxycycline treatment or in non-tyrosinase-tagged tumors (Fig. 7).

In terms of multimodality imaging, other than bimodal MR/PA imaging by Zemp et al. as mentioned above, Qin et al. [48] also evaluated the use of tyrosinase as a reporter gene for trimodal MR/PA/PET imaging. Melanin-targeting N-(2-(diethylamino)ethyl)-18F-5-fluoropicolinamide was used as a PET contrast agent and *in vivo* PA/MR/PET imaging studies showed higher contrast in tyrosinase-tagged tumors, as compared to non-tyrosinase-tagged tumors. This system offers complimentary benefits in terms of high sensitivity for both PA and PET imaging, as well as high contrast in T1-weighted MRI images. Moreover, in addition to possible multimodality imaging, Stritzker et al. [21] also demonstrated that

tyrosinase-induced melanin can also be used as a theranostic probe, via transduction into the recipient genome by an oncolytic vaccinia virus. In addition to providing MR/PA diagnostic contrast, this system can be used for laser-induced therapy and enhanced oncolytic viral therapy, thus demonstrating the potential of tyrosinase to be used as a reporter gene with multimodality and multifunctional capabilities. On the other hand, Ntziachristos and coworkers [49] also demonstrated the use of transfected red fluorescent proteins (iRFPs) in glioma brain tumors via multimodal fluorescence/CT/MSOT imaging.

In summary, reporter gene-based PAI can have a significant impact in the study of biological phenomena such as protein–protein interactions, changes in gene expression and signal transduction mechanisms, in order to further understand disease mechanisms, as well as monitor disease progression.

2.3 *Activatable Contrast Agents*

Over the past decade, various optical smart activatable probes have been designed for fluorescence imaging based on several activation mechanisms, such as enzymes, nucleic acids, pH, etc. [50]. These probes alter their optical properties upon activation and can be localized nonspecifically, since the detection mechanism is based on the variation in optical properties brought about by the target. This means that the probe signal-to-noise ratio is not limited by targeting efficiency, which can offer improved imaging contrast. However, these activatable probes still suffer from drawbacks such as tissue autofluorescence and low penetration depth, as is typical with conventional fluorescent probes.

More recently, several research groups have looked into extending this mechanism of signal activation into the field of PAI. For instance, Gambhir and coworkers [51] have developed an activatable PA probe based on two-wavelength imaging. Before matrix metalloproteinase (MMP-2) enzymatic cleavage, the dimerized probe, an activatable cell penetrating peptide labeled with two chromophores, black hole quencher (BHQ3) and Alexa750, shows PA signal at the two wavelengths corresponding to the absorption maxima of the two chromophores, 675 and 750 nm. After the cleavage, the dye associated with the cell-penetrating part of the probe, BHQ3, localizes in the cells, while the other dye diffuses away, resulting in PA signal seen at only one of the wavelengths, 675 nm. This probe has been employed in preclinical PA molecular imaging of follicular thyroid carcinoma (FTC), using MMPs as biomarkers for malignant thyroid lesions [52]. In general, the major requirements for selecting the chromophores are high absorption in the NIR region for high contrast deep tissue imaging, as well as well-differentiated, non-overlapping absorption spectra for proper spectral unmixing. By selecting chromophores and peptide backbone, the probe can be customized towards the target protease as well as to the imaging window. In this context, others have extended this two-wavelength imaging concept towards other chromophores, such as Yang et al. [53]. In particular, Yang conjugated BHQ3 to NIR-absorbing copper

sulfide (CuS) nanoparticles via a MMP-cleavable peptide linker. The resulting nanoconstruct exhibits two distinct absorption peaks at 630 and 930 nm. Within the MMP-rich tumor vicinity, upon MMP enzymatic cleavage, BHQ3, being a small molecule, was released and cleared from the tumor, whereas the larger CuS nanoparticles were retained within the tumor for a longer time. As a result, the PA signal at 680 nm from BHQ3 was minimized while that at 930 nm from CuS persisted. Thus, the PA signal ratio of 680 nm/930 nm could serve as an indicator of *in vivo* MMP activity within the tumor. Moreover, Gambhir and coworkers [54] have also developed a molecular probe, which upon proteolytic processing localizes at furin-active sites, thus providing PA contrast. The probe undergoes condensation-based oligomerization, followed by formation of aggregates and nanostructures, which accumulate at the target cells and tumor that express the protease, as shown in Fig. 8. This capability to augment tumor signals with activatable oligomerizable probes offers potential for PAI in protease activity detection.

On the other hand, Ntziachristos and coworkers [55] have demonstrated 3D volumetric mapping of MMP activity in human carotid specimens, via MSOT imaging coupled with a MMP-sensitive activatable probe, MMPsense™ 680. Since upregulated MMP expression is typically correlated with atherosclerotic plaque instability, this method can be used to characterize vulnerable plaque formation in atherosclerotic diseases, which is crucial for diagnostic monitoring and staging of plaque vulnerability, thus impacting therapeutic clinical decision making.

In addition, researchers have also looked into other triggering mechanisms for PA signal activation. For instance, Morgounova et al. [24] proposed a dimer-monomer contrast mechanism in the design of an enzyme-specific activatable probe. In essence, the probe comprises of two methylene blue (MB) molecules conjugated to each other via a peptide linkage in a dimer configuration. This configuration results in static quenching of the probe, producing short PA lifetime signal. The cleavage of the peptide linkage via endogenous enzymes separates the probe into MB monomers, enhancing the PA lifetime. This method offers high sensitivity, due to the lack of other long-lifetime molecules in the body. In summary, the system can be used to selectively detect activated MB monomers, which in turn provides a map of both enzyme location and activity. In addition, Jeon et al. [25] incorporated microbubbles, a standard ultrasound contrast agent, into MB solution which is PA active, in order to form a bimodal contrast solution. During propagation, the PA waves are attenuated by the surrounding microbubbles, suggesting that changing the microbubble concentration can be used to modulate the PA signal. Moreover, high-powered ultrasound can also be used to burst the microbubbles, which significantly improve PA contrast by more than 800 times and thus, offering a novel method for spatiotemporal control of PA signal generation.



Fig. 8 PAI of furin-like activity in tumor-bearing mice. **a** Photograph of a mouse placed in a positioning device for PA imaging; the subcutaneous tumor is positioned in the dimple. The *dotted yellow line* corresponds to the upper part of the tumor images shown in **(d)**. Variation of the PA signal with time after injection of 25 nmoles furin probe ESOR-PA01 via tail vein in either mice carrying **b** LoVo (furin-negative) or **c** MDA-MB-231 (furin-positive) tumors. PA signal was normalized to t = 0 min preinjection time point; n = 4, error bars, SD. **d** PA MIP images of mice tumors visualized in Amide software, acquired for 11 min at t = 0 min (preinjection) and t = 60 min after furin probe injection. **e** Increase of the PA signal quantified from 3D volumetric data of mice tumors, either from furin probe ESOR-PA01 injection in mice carrying LoVo (n = 4) and MDA-MB-231 (n = 4) tumors, or furin negative probe ESOR-PA02 in mice carrying MDA-MB-231 tumors (n = 4). The data represent the PA signal increase at t = 60 min post-probe injection relative to the pre-probe injection signal (t = 0); **P = 0.01, *P = 0.03, n.s. P = 0.08; error bars, SD. (Reproduced with permission from [54])

2.4 Others

In addition to the above mentioned probes, researchers are also developing other classes of compounds as potential PA contrast agents, which include conjugated polymers, metal carbonyl-based and upconversion molecules, as well as multi-modal dye-nanoparticle constructs. For instance, Zha et al. [56] demonstrated for the first time, the use of polypyrrole nanoparticles as polymer-based contrast agents for PAI. These polypyrrole nanoparticles have a small size (46 nm in diameter) and are stabilized with hydrophilic polyvinyl alcohol which provides biocompatibility and reduces non-specific protein absorption, enabling them to have a long circulation time in the bloodstream. After intravenous administration of the nanoparticles, the PA images of the mouse vasculature exhibited improved contrast over intrinsic hemoglobin signal in blood, highlighting the potential of these nanoparticles as PA contrast agents. In addition, Liu and coworkers [57] also designed another conjugated polymer, PFTTQ, via Suzuki polymerization, and encapsulated this polymer into a DSPE-PEG2000 matrix to yield water-soluble PFTTQ-loaded nanoparticles. These nanoparticles exhibited strong absorption in the 700–850 nm NIR range, as well as high photostability under continuous laser irradiation. In addition, these nanoparticles have been successfully utilized to image the rat brain vasculature with high PA contrast. Further bioconjugation of these nanoparticles with specific targeting ligands can also offer targeted *in vivo* imaging. In this context, Balasundaram et al. [58] developed a folate-targeting probe based on this polymer, for *in vivo* targeted PAI of breast cancer. In particular, they injected the folate-targeting probe into a folate receptor-positive MCF-7 breast cancer xenograft model, monitored the tumor localization and biodistribution of the probe over time, and compared the results with those from injecting the non-targeting probe with no folate moieties. The folate-targeting probe accumulated at the tumor site as early as 1 h post-injection and exhibited approximately 4 times higher contrast than that from the non-targeting probe (Fig. 9), thus demonstrating the great potential of this active-targeting polymer-based probe to be used as a PA contrast agent in biomedical applications.

In addition, Rao and team [59] developed semiconducting polymer nanoparticles as a novel class of PA contrast agents. These nanoparticles possess strong PA signals, high structural flexibility, narrow PA spectral profiles, as well as high chemical and photo-stabilities. Thus, in this study, they have been successfully demonstrated whole-body lymph node PA mapping in mice, as well as ratiometric PAI of reactive oxygen species in living mice.

On the other hand, Kong et al. [60] reported, for the first time, the use of water-soluble organometallic carbonyl clusters as PA contrast agents. These clusters offer strong PA signals, high chemical stability, as well as low toxicity, and

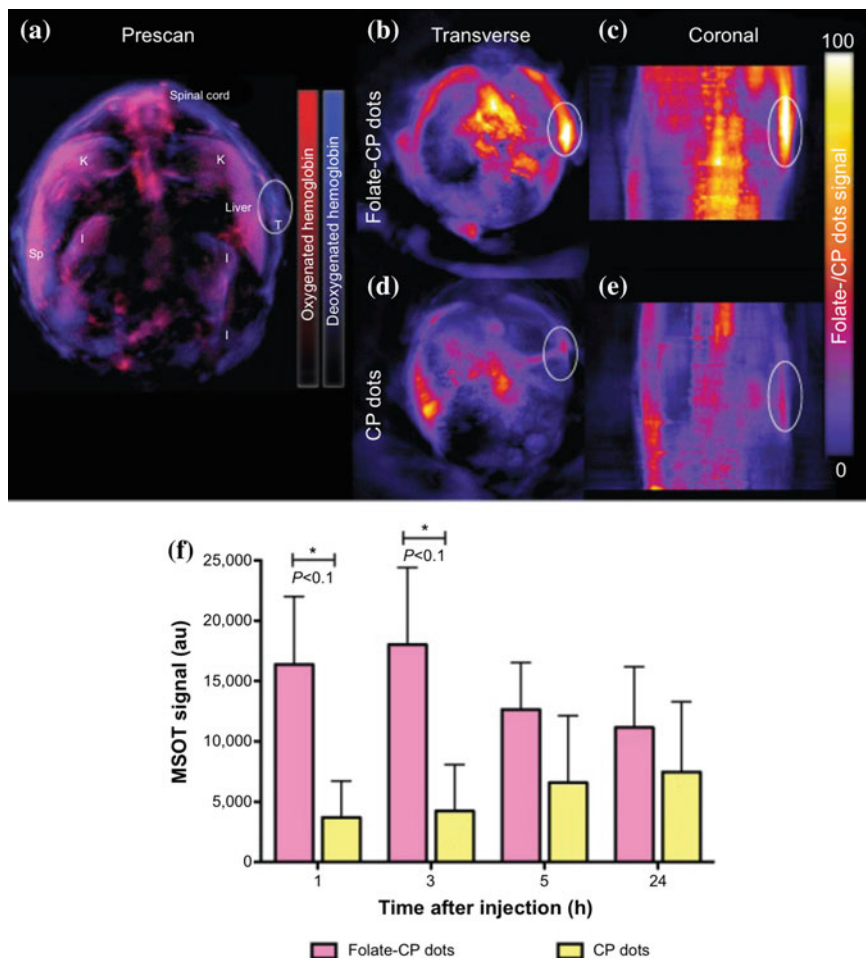


Fig. 9 Molecular PAI of breast cancer. MSOT MIP images of cross-sectional abdomen before systemic administration of the probe (a), at 3 h after systemic administration of folate-CP dots in b transverse and c coronal views and CP dots in d transverse and e coronal views. The white ellipse indicates the tumor location. f PA signal quantification by ROI analysis at the tumor site after systemic probe administration in folate-positive MCF-7 breast cancer tumor model. CP Conjugated polymer; Sp spleen; I intestine; K kidneys; T tumor. (Reproduced with permission from [58])

they can be easily biofunctionalized with ligands for targeted detection. In this study, they injected these clusters into rats and imaged the cerebral cortex vasculature in vivo using dark-field PAM. In addition, Maji et al. [61] also demonstrated, for the first time, the use of a water-soluble upconversion nanoparticle- α -CD inclusion complex (UC- α -CD) for in vivo PAI. Upon 980 nm excitation, UC- α -CD dispersed in water shows luminescence quenching via solvent-induced

non-radiative relaxation, and an increase in thermal conductivity, which in turn leads to subsequent PA signal enhancement, both in phantoms *ex vivo* and in mice *in vivo*. Moreover, Dinish et al. [62] also developed multimodal dye-gold nanoparticle conjugates for both SERS biosensing and PAI of cancer biomarkers *in vivo*.

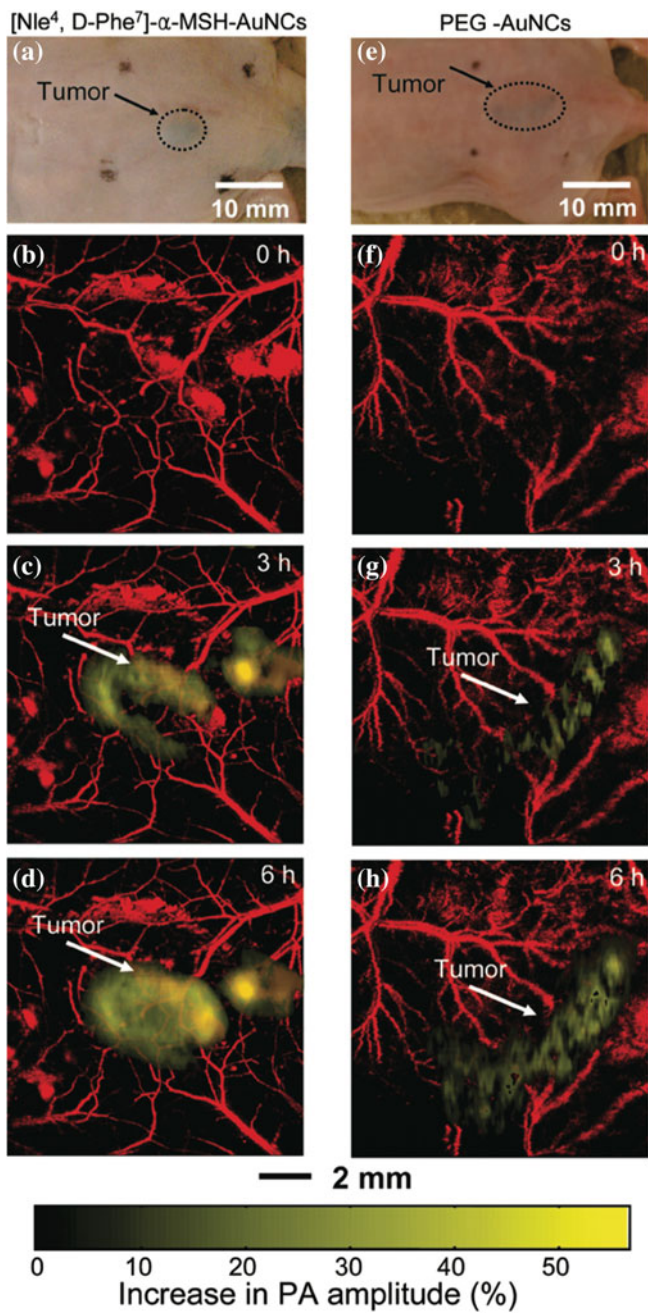
3 Preclinical Applications

PAI for biomedical applications has seen tremendous growth in the last few years, which is primarily due to its ability to interrogate optical absorption in deep tissue organs with micrometer resolution. Moreover, it provides molecular, functional and anatomical imaging capabilities at clinically relevant depths for *in vivo* applications, which makes the technique versatile and unique. Among the various applications, PAI has shown tremendous advancement in preclinical research, and also presented itself as an effective translational imaging modality. In this section, we provide an overview of cutting-edge preclinical applications in tumor, skin and brain imaging.

3.1 Cancer Imaging

PAI has shown great promise in providing structural, functional and molecular information simultaneously for many preclinical studies [63]. In tumor imaging, PAI can be used to successfully visualize tumor location located within deep tissue, provide information on tumor vasculature [64], as well as monitor angiogenesis [65]. Moreover, information on oxygen saturation at high resolution can also be obtained using PAI coupled with the endogenous chromophore, hemoglobin.

Endogenous chromophores in the body such as melanin and hemoglobin are used as optical markers for cancer detection. The PA signal from the higher melanin concentration at the tumor location relative to the surrounding tissue was effectively used for melanoma detection using PAM [64, 66, 67]. Tumor detection using PA imaging can also be achieved due to the presence of dense vasculature at the tumor location compared to that of normal tissues, which enhances the PA contrast. In this direction, Ku et al. demonstrated the detection of tumor angiogenesis in the rat brain using PA tomography (PAT) [68]. PAI can be used to detect tumor vasculature at higher resolution than other vascular imaging techniques such as MRI, CT or PET [63]. Further, hypoxia in tumors can be detected by measuring the oxygen content in the blood [69]. The level of blood oxygen saturation can be estimated from the ratio of PA signal intensities from oxy- and de-oxy hemoglobin, which have distinct optical absorption profiles.



◀ **Fig. 10** Photographs of nude mice transplanted with melanomas (a) before injection of bioconjugated AuNCs and control PEG-encapsulated-AuNCs (e). Time-course PA images of melanomas after intravenous injection with 100 μ L of 10 nM conjugated AuNCs (b–d) and control PEG-AuNCs (f–h) through the tail vein. The background vasculature images were obtained using the PA microscope at 570 nm (ultrasonic frequency of 50 MHz), and the melanoma images were obtained using the PAT at 778 nm (ultrasonic frequency = 10 MHz). Color schemes: *red* for blood vessels; *yellow* for PA amplitude increase. (Reproduced with permission from [74])

On the other hand, various exogenous contrast agents can be used to increase the sensitivity of PAI for tumor detection. Attaching various targeting moieties (such as peptides, aptamers and antibodies) to exogenous agents will provide specific molecular information regarding the tumor. In order to differentiate malignant cells from healthy cells, a sufficient concentration of exogenous contrast agents must reach the target for successful labelling within an appropriate time. Hence, the delivery, targeting efficacy, clearance and cytotoxicity are the main considerations for molecular probe designs. Various exogenous PA contrast agents, which include fluorescent dyes, gold nanoparticles (in various sizes and shapes), carbon-based materials, activatable probes, quantum dots, as well as polymers, have been used for tumor detection in orthotopic and xenograft models [58, 63, 70, 71]. Among these compounds, ICG and the photosensitizers offer great potential to be translated for clinical applications, as mentioned in the previous section.

3.2 Skin Imaging

The highly scattering nature of biological samples often limits the application of various optical techniques. However, in PA measurements, this limitation can be overcome because the detected signal is based on the direct absorption of the incident laser radiation. This salient feature drives PA as an efficient technique in the study of opaque materials and complex biological systems such as the skin. PA measurements can be employed to study skin absorption characteristics, skin disorders, topically applied products, as well as kinetic changes related to transdermal drug delivery [72].

In one of the earlier publications of PAI for skin applications, Zhang et al. [73] developed a dual modal PA and optical coherence tomography (PAT/OCT) scanner for in vivo imaging. The system is integrated with all optical detection schemes for both modalities in backward mode utilizing a shared 2D optical scanner with a field-of-view of $\sim 13 \times 13$ mm. Using this system, 3D in vivo images of the vasculature and the surrounding tissue micro-morphology in murine and human skin were acquired at a depth of up to ~ 5 mm. Wang and team [74] demonstrated the successful imaging of melanoma in a mouse model by combining high-resolution PAT along with gold nanocages (AuNCs). They used bio-conjugated AuNCs with α -melanocyte-stimulating hormone for the imaging of melanomas with high sensitivity and specificity as shown in Fig. 10. Furthermore, simultaneous functional PAI

of oxygen saturation was also successfully achieved, in order to reveal the physiological states of the melanomas.

3.3 *Brain Imaging*

PAI of the brain is an upcoming research area, which can act as a complementary imaging modality with magnetic resonance imaging (MRI) in future translational medicine. In one of the pioneering studies, Wang and team [75] demonstrated that PAT can be used for *in vivo* noninvasive transdermal and transcranial imaging of the structure and function in the rat brain. They could accurately map the rat brain structures and functional hemodynamic changes in cortical blood vessels around the whisker-barrel cortex, in response to stimulation as shown in Fig. 11. They were also successful in imaging the hyperoxia and hypoxia-induced cerebral hemodynamic changes. As a continuation of this work, the same research team demonstrated the simultaneous transcranial imaging of two functional parameters, the total hemoglobin concentration and oxygen saturation in the rat brain *in vivo* through the intact skin and skull [76]. They could image the blood volume and oxygenation in the cortical venous vessels, altered by systemic physiological modulations such as hyperoxia, normoxia, and hypoxia.

Ntziachristos and team [77] employed MSOT for high-resolution brain imaging and glioblastoma characterization in a mouse model. They used endogenous oxy- and deoxy-hemoglobin, as well as exogenous ICG for the simultaneous anatomical, functional and molecular imaging of the brain. In addition, ICG was used for the real-time study of the kinetics of uptake and clearance in the brain vasculature. They could also achieve successful imaging of tumor growth in the U87 glioblastoma model, visualized through the intact skull by monitoring the changes in deoxygenated hemoglobin at the tumor site. In the future, this MSOT imaging modality may provide a new paradigm in preclinical small animal brain imaging and characterization, via the study of physiological and targeted molecular signals with very high resolution, which is not possible by other optical imaging modalities.

On the other hand, the difficulty in delineating brain tumor margins is a major obstacle in the path toward better outcomes for patients with brain tumors. Towards overcoming this limitation, Gambhir and team [78] developed a unique triple-modality MRI-PAI-Raman nano-construct, which can be used to delineate the margins of brain tumors in a glioblastoma model both pre-operatively and intra-operatively. This triple-modality nano-construct was detected with picomolar sensitivity both *in vitro* and in living mice, with high tumor retention, allowing for noninvasive tumor delineation using all three modalities through the intact skull.

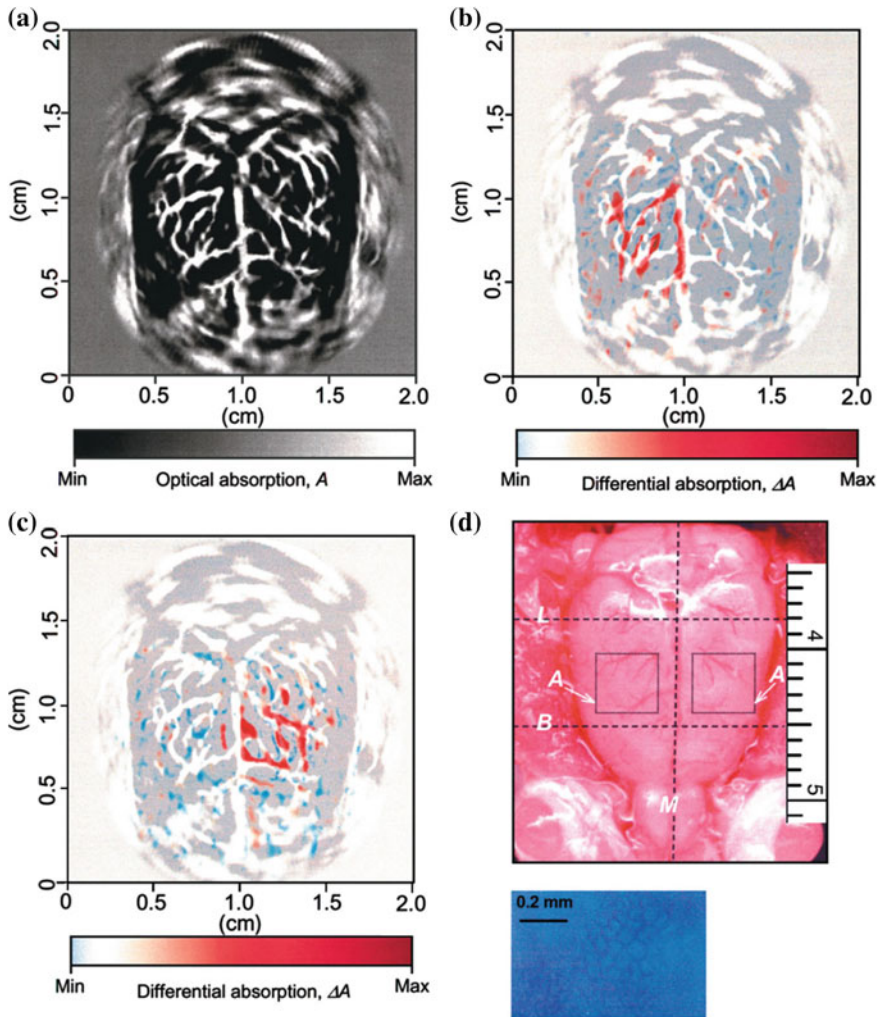


Fig. 11 Functional imaging of cerebral hemodynamic changes in response to whisker stimulation. **a** Noninvasive PA image of the vascular pattern in the superficial layer of the rat cortex acquired with the skin and skull intact. **b, c** Noninvasive functional PA images acquired after *left-* and *right-* side whisker stimulation respectively, with the skin and skull intact. These two functional maps are overlaid on the vascular image in the superficial cortex shown in **(a)**. **d** Open-skull photograph of the rat cortical surface. B, bregma; L, lambda; M, midline; A, activated regions corresponding to whisker stimulation (4 × 4 mm). **e** Histology of normal lamina IV cortical barrels, located in regions in A, representing the large mystacial vibrissae of the rat somatosensory system (40 × magnification). (Reproduced with permission from [75])

4 Clinical Applications

PAT offers anatomical, functional and molecular contrast at high resolution at depths up to 4–5 cm, while avoiding the high cost and extensive infrastructure associated with other modalities such as PET and MRI. In addition, PA contrast is purely optical and hence does not require ionizing radiation, as required for CT and PET. PAT therefore offers attractive advantages to clinicians in disease diagnosis.

As above, there are two strategies that enable clinical assessment with PA. Firstly, contrast derived from intrinsic chromophores can provide important information about disease status. In order to maximize imaging depth, excitation is typically conducted in the NIR window where overall tissue absorption is relatively low. Within the NIR, multiple intrinsic chromophores such as hemoglobin, melanin and lipids have characteristic absorption profiles on which PAI capitalizes to provide contrast. The relative concentration of deoxygenated and oxygenated hemoglobin, for example, allows the determination of oxygen saturation in blood vessels and tissues. Oxygen saturation is an important parameter in diseases involving ischemia, hypoxia or hypoxemia. The distribution of melanin, another strong broadband absorber, is important in the imaging of melanoma and hair follicles. Lipids also have a characteristic absorption, the magnitude of which surpasses water above 1200 nm, allowing visualization of arterial plaques and sebaceous glands. In addition to intrinsic chromophores, administered contrast agents provide targeted and non-targeted enhancement of PA signals. These agents provide information about perfusion and can be conjugated to small molecules and peptides for molecular specificity. As reviewed above, ICG is the only dye with significant absorption in the NIR that has FDA approval for clinical use. Other agents are used routinely for small-scale experimental clinical studies, but are not yet approved for general use. The aforementioned sources of contrast, in addition to the imaging depth possible with PA, define the scope of possible clinical applications. Zackrisson et al. [79] have illustrated broad potential clinical applications, which take advantage of both intrinsic and extrinsic sources of contrast.

Based on these possibilities, a number of registered clinical trials using PA are ongoing or have been completed. In the United States alone, for example, there are 14 registered clinical trials, including patients with rheumatoid arthritis, melanoma, Port-wine birthmarks, diabetic macular edema, breast cancer, prostate cancer, ovarian cancer, and rectal cancer [2]. The availability of approved contrast agents provides the most significant regulatory hurdle to the broad use of PA in clinical imaging. Until more agents are approved, clinical diagnosis using PA will rely on the intrinsic chromophores described above and various approaches capitalizing on ICG. The process of development and approval for new contrast agents are significant endeavors, as some have estimated that it costs \$100–\$200 million and takes 8–10 years for the translation of a new discovery to an imaging agent commercially available on the market [80]. Based on this reality, the remainder of this section will focus on specific examples of clinical applications using intrinsic contrast, or the clinically approved ICG.

4.1 *Melanoma Detection*

PA detection of melanin was first described in 1990 by conducting spectroscopy on synthetic melanin [81]. This application was extended to animals, where label-free tumor melanin distribution was characterized in B16 skin melanoma tumor-bearing mice [67]. Pilot studies are currently assessing the utility of using PAI to characterize the primary lesion in melanoma patients. The staging of melanoma is dependent in part on the tumor depth, which is typically characterized by histological assessment of a biopsy or the excised primary tumor. Additional parameters from histology are also used. Evaluation must be performed by an experienced pathologist, which takes time. However, a non-invasive approach like MSOT of defining tumor depth in melanoma patients would provide rapid screening with real-time feedback to the physician during an in-patient procedure.

4.2 *Sentinel Lymph Node Mapping*

A major mechanism of tumor metastasis involves transit of tumor cells from the primary lesion to distant sites through draining lymph nodes [82], termed sentinel lymph nodes (SLN). SLN identification and evaluation is therefore paramount in staging cancer, since the presence of lymph nodes containing cancer cells is associated with a higher risk of metastasis and mortality. The current gold standard for SLN assessment is the injection of a radioactive tracer at the site of the primary tumor with subsequent lymphoscintigraphy. This approach creates a radioactive burden for the clinician and patient.

A preferred alternative will be to avoid the use of radioactivity and simplify the requirements for imaging, but still retain the ability to assess all relevant lymph node basins. The feasibility of ICG-mediated detection of the SLN via MSOT was demonstrated in animals [83]. In addition, twelve lymph nodes from eight melanoma patients were scanned *ex vivo* using a Vevo LAZR multispectral photoacoustic imager, out of which melanoma metastases could be identified [84].

4.3 *Breast Cancer Imaging*

Pilot studies in mice have shown the capacity of PAI to assess folate receptor density in breast tumors established in mouse models [58]. Preliminary studies in humans using the laser optoacoustic imaging system (LOIS-64), which have since escalated into ongoing clinical trials, compared the utility of PAI against gold standards such as mammography and ultrasound imaging (Fig. 12) [85]. In these studies, multiple defining aspects of growing tumors, such as hyperactive metabolic

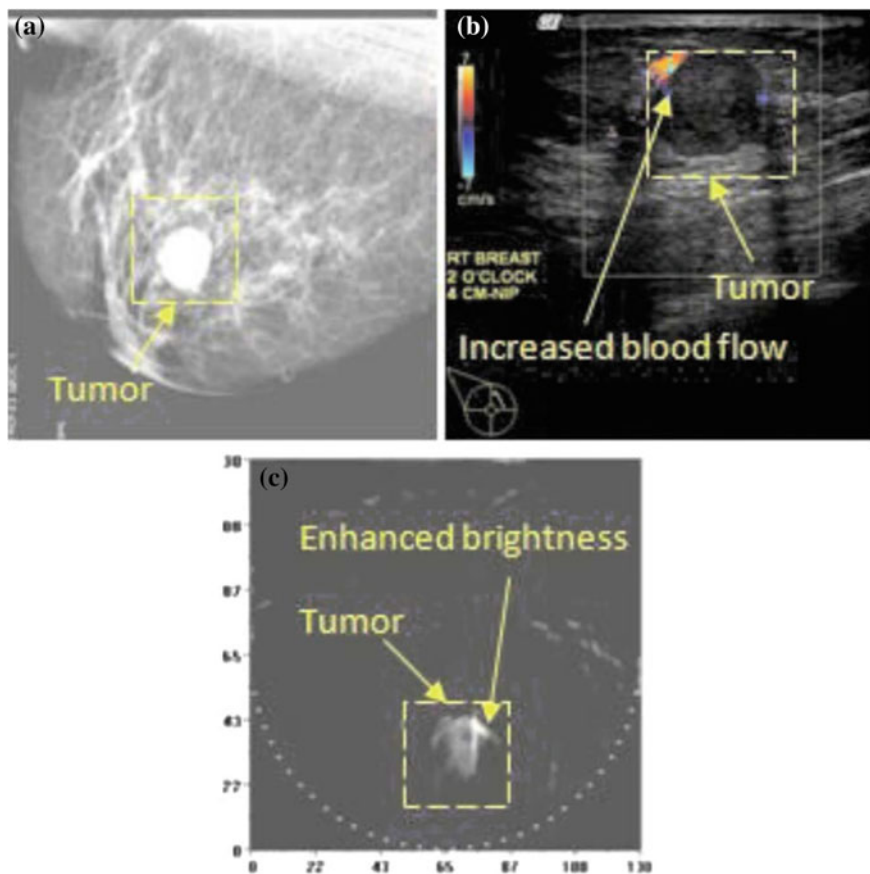


Fig. 12 **a** Digital mammography image (mediolateral projection) of the breast, showing a round, apparently benign tumor. **b** Ultrasonic imaging with the Doppler showing the tumor boundaries and the focal blood flow increase. **c** Optoacoustic image (mediolateral projection) showing the enhanced contrast around the area of the focal blood flow increase detected by the Doppler ultrasound. (Reproduced with permission from [85])

state, angiogenesis, irregular vessel architecture, oxygenation status, and possible necrosis, are utilized to generate PA metrics of tumor presence and status.

4.4 Cardiovascular Disease Monitoring

In patients with peripheral vascular disease, gold standard diagnostic methods include the palpation of the extremities and duplex ultrasonography. In some patients, angiography provides additional insight into the presence and location of vascular blockages. The former method provides subjective information, while the

other methods provide information related to blood flow and the structure of larger blood vessels. However, little information is available on the status of microvasculature. Herein lies the promise of PAI, which can quantify oxygenation and perfusion with high spatial resolution. A recent study [86] conducted on healthy human volunteers compared duplex ultrasound and MSOT, showing that PA can assess vasculature that is too small to be seen by conventional ultrasound.

In addition, pilot studies have also considered the feasibility of imaging the human common carotid artery as well as the internal and external jugular veins [87]. The ability to access and quantify oxygenation in these commonly studied, large blood vessels deep in tissue, in addition to having access to microvasculature that is otherwise invisible to current gold standard imaging methods, demonstrates that MSOT is an attractive supplement for clinical imaging of vascular disease.

4.5 *Skin Imaging*

Current methodologies for the assessment of hair and scalp diseases such as alopecia areata, female androgenic alopecia, monilethrix and Netherton syndrome involve dermatoscopy (i.e. a handheld low-magnification light microscope) and analysis of hair or tissue samples removed forcibly or via biopsy. However, current technology limits the non-invasive assessment of the morphology of a hair follicle, the oxygenation status of the capillary bed surrounding the hair papilla and the content of the pilosebaceous unit. With the use of a high-resolution PAI system equipped with laser excitation including wavelengths of high lipid contrast, this gap in the available methodologies can be bridged (Fig. 13) [88].

Applications of MSOT imaging in dermatology also extend to wound healing, for example, in the case of diabetic patients who suffer from chronic wounds and ulcers. By using PAI to assess oxygenation in the wound biofilm, as well as its thickness, ongoing research hopes to stratify at-risk patients and those who are responding to therapy. In addition to studying wounds, PA has also shown promise in imaging burn patients. For example, Ida et al. [89] could distinguish skin layers from underlying muscle and subserosal tissue, and they monitored changes in PA signals in a rat burn model 5 days post injury. Similarly, different skin layers could be distinguished in human healthy volunteers [90], and burns were also assessed in rodent samples and human healthy volunteers [91]. These proof-of-principle studies indicate a potential for PAI to provide important clinical information for patients with chronic wounds and burns. High resolution skin imaging, down to 4 micron axial resolution, at superficial depths has been enabled by means of raster scanning optoacoustic microscopy (RSOM), which uses high-frequency acoustic transducers and a scanning approach to deliver highly resolved imaging of vasculature in the dermis [92].

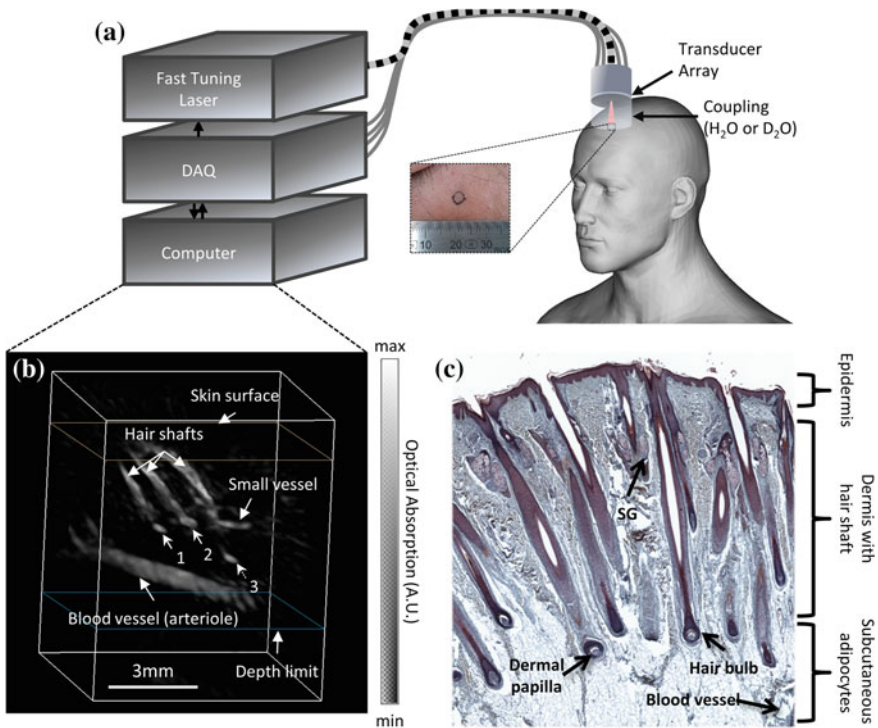


Fig. 13 Handheld PA probe for high resolution real-time imaging of hair follicles. **a** Schematic of the imaging system and approach. **b** Representative 3D PA image, demonstrating general physiological structures below the skin surface, including the hair shafts and bulbs, dermal papilla (indicated by numbered arrows), and a deeper, larger blood vessel. The dermal papilla appear to be detached in hairs marked by arrow 3, suggesting this follicle may be in the catagen or telogen phase, whereas the dermal papillae of the hairs marked by arrows 1 and 2 appear to be attached, suggesting these follicles are in an anagen phase. **c** Representative Masson's Trichrome microscope image (at 10 \times magnification) from paraffin embedded scalp hair of a healthy individual. When compared with the PA images, it reveals similar structures, namely the dermal papilla, hair shafts and bulbs, and a large subcutaneous blood vessel. The hair bulbs and dermal papilla are located at some places in the subcutaneous fat tissue. Note that also visible in the histological image are sebaceous glands (SG) in the dermis close to the skin surface. (Reproduced with permission from [88])

4.6 Arthritis Imaging

Arthritis patients also represent a clinical population that could benefit from PAI. Joint inflammation is often assessed by a physician through appearance, palpation, and patient interviews. In contrast, non-invasive imaging provides a more thorough and unbiased assessment of joint pathology. In this context, MRI is the preferred imaging modality. As discussed above, MRI requires substantial investment and infrastructure, as well as dedicated personnel for its operation and data

management. On the other hand, PAI offers a simpler approach to assess joint integrity and inflammation. In a recent pilot study in mice, the ability of MSOT to differentiate animals based on the extent of disease was assessed using MRI as a gold standard [93]. In this study, ICG retention in the joint of affected animals was used as a surrogate disease marker, based on the principle of enhanced permeability and retention. This concept was extended to human arthritis patients, where ICG accumulation in finger joints was used as an indicator of disease status [94].

5 Conclusions and Future Perspectives

Over recent years, there have been great technological advances in optoacoustic imaging instrumentation, data processing, contrast agents, as well as preclinical and clinical applications. Wide-ranging instrumentation has been developed in various form factors, enabling microscopic, mesoscopic, endoscopic, as well as tomographic imaging. The early part of this chapter has focused on MSOT implementation, which combines tomographic detection with multispectral imaging and processing to obtain concentration maps of chromophores within deep tissue. Multiple transducer designs, image reconstruction and spectral unmixing algorithms have been discussed in depth. Future hardware development will comprise the development of more sensitive detectors and more powerful lasers, whereas software development will include coming up with novel algorithms that can offer improvement in quantification accuracy in the image reconstruction and spectral unmixing processes, as well as reductions in acoustic artifacts.

Alongside with instrumentation development, a great myriad of PA contrast agents have also been developed, in order to improve contrast, provide active targeting and acquire multimodal and multifunctional capabilities. In particular, clinically relevant fluorophores such as photosensitizers and ICG, genetic reporters, activatable contrast agents, as well as upcoming novel classes of PA contrast agents have been covered in greater detail in this chapter.

In terms of applications, PAI has demonstrated tremendous advancement within the past few years, primarily due to its ability to perform simultaneous high-resolution anatomical, functional and molecular imaging in deep tissue. In addition, it is purely optical with non-ionizing radiation and thus, safe for patients. All these advantages have led to the use of PAI in various preclinical and clinical applications, which include tumor, skin, brain, lymphatic, cardiovascular imaging, and many others.

In summary, the field of PAI is continuously growing. While publication of preclinical imaging studies can be traced back more than 10 years, clinical studies have only just begun to emerge. Indeed, 2014 saw the first CE-marked PAI system for breast cancer patients (Seno Medical Instruments, Inc.), and in 2015 additional CE and FDA approval of a PAI system as a medical product is expected for

commercial products from other companies like iThera Medical. This will allow assessment of whether scientific potential can meet clinical reality, and whether PAI can provide new clinical insights into disease development, diagnosis, and therapeutic responses.

References

1. A.G. Bell, On the production and reproduction of sound by light. *Am. J. Sci.* **20**, 305–324 (1880)
2. A.G. Bell, Upon the production of sound by radiant energy. *Philos. Mag.* **11**, 510 (1881)
3. J. Xia, J. Yao, L.V. Wang, Photoacoustic tomography: principles and advances. *Electromagnetic Waves (Cambridge)* **147**, 1–22 (2014)
4. V. Ntziachristos, Going deeper than microscopy: the optical imaging frontier in biology. *Nat. Methods* **7**, 603–614 (2010)
5. S. Kellnberger, A. Hajiaboli, D. Razansky, V. Ntziachristos, Near-field thermoacoustic tomography of small animals. *Phys. Med. Biol.* **56**(11), 3433–3444 (2011)
6. R. Ma, S. Söntges, S. Shoham, V. Ntziachristos, D. Razansky, Fast scanning coaxial optoacoustic microscopy. *Biomed. Opt. Express* **3**(7), 1724–1731 (2012)
7. M. Schwarz, M. Omar, M. Buehler, J. Aguirre, V. Ntziachristos, Implications of ultrasound frequency in optoacoustic mesoscopy of the skin. *IEEE Trans. Med. Imaging* **34**(2), 672–677 (2014)
8. L.V. Wang, L. Gao, Photoacoustic microscopy and computed tomography: from bench to bedside. *Ann. Rev. Biomed. Eng.* **16**, 155–185 (2014)
9. V. Ntziachristos, D. Razansky, Molecular imaging by means of multispectral optoacoustic tomography (MSOT). *Chem. Rev.* **110**(5), 2783–2794 (2010)
10. S.E. Bohndiek, S. Bodapati, D. van de Sompel, S.R. Kothapalli, S.S. Gambhir, Development and application of stable phantoms for the evaluation of photoacoustic imaging instruments. *PLoS ONE* **8**(9), e75533 (2013)
11. R. Su, S. Ermilov, A. Liopo, A. Oraevsky, Laser optoacoustic tomography: towards new technology for biomedical diagnostics. *Nucl. Instrum. Methods Phys. Res., Sect. A* **720**, 58–61 (2013)
12. A. Needles, A. Heinmiller, J. Sun, C. Theodoropoulos, D. Bates, D. Hirson, M. Yin, F.S. Foster, Development and initial application of a fully integrated photoacoustic micro-ultrasound system. *IEEE Trans. Ultrason. Ferroelectr. Freq. Control* **60**(5), 888–897 (2013)
13. A. Rosenthal, S. Kellnberger, M. Omar, D. Razansky, V. Ntziachristos, Wideband optical detector of ultrasound for medical imaging applications. *J. Vis. Exp.* **87**, e50847 (2014)
14. A. Rosenthal, V. Ntziachristos, D. Razansky, Acoustic inversion in optoacoustic tomography: a review. *Curr. Med. Imaging Rev.* **9**(4), 318–336 (2013)
15. A. Rosenthal, V. Ntziachristos, D. Razansky, Model-based optoacoustic inversion with arbitrary-shape detectors. *Med. Phys.* **38**(7), 4285–4295 (2011)
16. D. Queirós, X.L. Déan-Ben, A. Buehler, D. Razansky, A. Rosenthal, V. Ntziachristos, Modeling the shape of cylindrically focused transducers in three-dimensional optoacoustic tomography. *J. Biomed. Opt.* **18**(7), 076014 (2013)
17. A. Rosenthal, T. Jetzfellner, D. Razansky, V. Ntziachristos, Efficient framework for model-based tomographic image reconstruction using wavelet packets. *IEEE Trans. Med. Imaging* **31**(7), 1346–1357 (2012)
18. S.L. Jacques, Coupling 3D Monte Carlo light transport in optically heterogeneous tissues to photoacoustic signal generation. *Photoacoustics* **2**(4), 137–142 (2014)

19. B.T. Cox, S.R. Arridge, K.P. Köstli, P.C. Beard, Two-dimensional quantitative photoacoustic image reconstruction of absorption distributions in scattering media by use of a simple iterative method. *Appl. Opt.* **45**(8), 1866–1875 (2006)
20. J. Glatz, N.C. Deliolanis, A. Buehler, D. Razansky, V. Ntziachristos, Blind source unmixing in multi-spectral optoacoustic tomography. *Opt. Express* **19**(4), 3175–3184 (2011)
21. J. Stritzker, L. Kirscher, M. Scadeng, N.C. Deliolanis, S. Morscher, P. Symvoulidis, K. Schaefer, Q. Zhang, L. Buckel, M. Hess, U. Donat, W.G. Bradley, V. Ntziachristos, A.A. Szalay, Vaccinia virus-mediated melanin production allows MR and optoacoustic deep tissue imaging and laser-induced thermotherapy of cancer. *Proc. Natl. Acad. Sci.* **110**(9), 3316–3320 (2013)
22. S. Tzoumas, N. Deliolanis, S. Morscher, V. Ntziachristos, Un-mixing molecular agents from absorbing tissue in multispectral optoacoustic tomography. *IEEE Trans. Med. Imaging* **33**(1), 48–60 (2013)
23. J.F. Lovell, T.W.B. Liu, J. Chen, G. Zheng, Activatable photosensitizers for imaging and therapy. *Chem. Rev.* **110**, 2839–2857 (2010)
24. E. Morgounova, Q. Shao, B.J. Hackel, D.D. Thomas, S. Ashkenazi, Photoacoustic lifetime contrast between methylene blue monomers and self-quenched dimers as a model for dual-labeled activatable probes. *J. Biomed. Opt.* **18**(5), 056004/1-9 (2013)
25. M. Jeon, W. Song, E. Huynh, J. Kim, J. Kim, B.L. Helfield, B.Y.C. Leung, D.E. Goertz, G. Zheng, J. Oh, J.F. Lovell, C. Kim, Methylene blue microbubbles as a model dual-modality contrast agent for ultrasound and activatable photoacoustic imaging. *J. Biomed. Opt.* **19**(1), 016005/1-9 (2014)
26. Q. Shao, E. Morgounova, C. Jiang, J. Choi, J. Bischof, S. Ashkenazi, In vivo photoacoustic lifetime imaging of tumor hypoxia in small animals. *J. Biomed. Opt.* **18**(7), 076019/1-9 (2013)
27. A. Hirao, S. Sato, D. Saitoh, N. Shinomiya, H. Ashida, M. Obara, In vivo photoacoustic monitoring of photosensitizer distribution in burned skin for antibacterial photodynamic therapy. *Photochem. Photobiol.* **86**, 426–430 (2010)
28. S. Stolik, S.A. Tornás, E. Ramón-Gallegos, A. Cruz-Orea, F. Sánchez-Sinencio, Determination of aminolevulinic-acid-induced protoporphyrin IX in mice skin. *Rev. Sci. Instr.* **74**(1), 374–377 (2003)
29. A. Abuteen, S. Zanganeh, J. Akhigbe, L.P. Samankumara, A. Aguirre, N. Biswal, M. Braune, A. Vollertsen, B. Röder, C. Brückner, Q. Zhu, The evaluation of NIR-absorbing porphyrin derivatives as contrast agents in photoacoustic imaging. *Phys. Chem. Chem. Phys.* **15**, 18502–18509 (2013)
30. D. Zhang, Y.-X. Zhao, Z.-Y. Qiao, U. Mayerhöffer, P. Spent, X.-J. Li, F. Würthner, H. Wang, Nano-confined squaraine dye assemblies: new photoacoustic and near-infrared fluorescence dual-modular imaging probes in vivo. *Bioconjug. Chem.* **25**(11), 2021–2029 (2014)
31. M. Frenette, M. Hatamimoslehadi, S. Bellinger-Buckley, S. Laoui, J. La, S. Bag, S. Mallidi, T. Hasan, B. Bouma, C. Yelleswarapu, J. Rochford, Shining light on the dark side of imaging: excited state absorption enhancement of a bis-styryl BODIPY photoacoustic contrast agent. *J. Am. Chem. Soc.* **136**(45), 15853–15856 (2014)
32. A.B.E. Attia, G. Balasundaram, W. Driessen, V. Ntziachristos, M. Olivo, Phthalocyanine photosensitizers as contrast agents for in vivo photoacoustic tumor imaging. *Biomed. Opt. Exp.* **6**, 591–598 (2015)
33. N. Bézière, V. Ntziachristos, Optoacoustic imaging of naphthalocyanine: potential for contrast enhancement and therapy monitoring. *J. Nucl. Med.* **56**(2), 323–328 (2015)
34. Y. Zhang, M. Jeon, L.J. Rich, H. Hong, J. Geng, Y. Zhang, S. Shi, T.E. Barnhart, P. Alexandridis, J.D. Huizinga, M. Seshadri, W. Cai, C. Kim, J.F. Lovell, Non-invasive multimodal functional imaging of the intestine with frozen micellar naphthalocyanines. *Nature Nanotech.* doi:[10.1038/NNANO.2014.130](https://doi.org/10.1038/NNANO.2014.130) (2014)
35. C.J.H. Ho, G. Balasundaram, W. Driessen, R. McLaren, C.L. Wong, U.S. Dinis, A.B.E. Attia, V. Ntziachristos, M. Olivo, Multifunctional photosensitizer-based contrast agents for photoacoustic imaging. *Sci. Rep.* **4**, 5342–5347 (2014)

36. E. Herzog, A. Taruttis, N. Bézière, A.A. Lutich, D. Razansky, V. Ntziachristos, Optical imaging of cancer heterogeneity with multispectral optoacoustic tomography. *Radiology* **263** (2), 461–468 (2012)
37. A. Buehler, E. Herzog, D. Razansky, V. Ntziachristos, Video rate optoacoustic tomography of mouse kidney perfusion. *Opt. Lett.* **35**(14), 2475–2477 (2010)
38. A. Taruttis, S. Morscher, N.C. Burton, D. Razansky, V. Ntziachristos, Fast multispectral optoacoustic tomography (MSOT) for dynamic imaging of pharmacokinetics and biodistribution in multiple organs. *PLoS ONE* **7**(1), e30491/1-6 (2012)
39. N. Bézière, N. Lozano, A. Nunes, J. Salichs, D. Queiros, K. Kostarelos, V. Ntziachristos, Dynamic imaging of PEGylated indocyanine green (ICG) liposomes within the tumor microenvironment using multi-spectral optoacoustic tomography (MSOT). *Biomaterials* **37**, 415–424 (2015)
40. G. Kim, S.-W. Huang, K.C. Day, M. O'Donnell, R.R. Agayan, M.A. Day, R. Kopelman, S. Ashkenazi, Indocyanine-green-embedded PEBBLEs as a contrast agent for photoacoustic imaging. *J. Biomed. Opt.* **1**(4), 044020/1-8 (2007)
41. S. Zanganeh, H. Li, P.D. Kumavor, U. Alqasemi, A. Aguirre, I. Mohammad, C. Stanford, M. B. Smith, Q. Zhu, Photoacoustic imaging enhanced by indocyanine green-conjugated single-wall carbon nanotubes. *J. Biomed. Opt.* **18**(9), 096006/1-11 (2013)
42. L. Li, R.J. Zemp, G. Lungu, G. Stoica, L.V. Wang, Photoacoustic imaging of lacZ gene expression in vivo. *J. Biomed. Opt.* **12**(2), 020504/1-3 (2007)
43. X. Cai, L. Li, A. Krumholz, Z. Guo, T.N. Erpelding, C. Zhang, Y. Zhang, Y. Xia, L.V. Wang, Multi-scale molecular photoacoustic tomography of gene expression. *PLoS ONE* **7**(8), 1–7 (2012)
44. A. Krumholz, S.J. VanVickle-Chavez, J. Yao, T.P. Fleming, W.E. Gillanders, L.V. Wang, Photoacoustic microscopy of tyrosinase reporter gene in vivo. *J. Biomed. Opt.* **16**(8), 080503/1-4 (2011)
45. R.J. Paproski, A.E. Forbrich, K. Wachowicz, M.M. Hitt, R.J. Zemp, Tyrosinase as a dual reporter gene for both photoacoustic and magnetic resonance imaging. *Biomed. Opt. Express* **2** (4), 771–780 (2011)
46. R.J. Paproski, A. Forbrich, T. Harrison, M. Hitt, R.J. Zemp, Photoacoustic imaging of gene expression using tyrosinase as a reporter gene. *Proc. SPIE* **7899**(78991H/1-7) (2011)
47. R.J. Paproski, A. Heinmiller, K. Wachowicz, R.J. Zemp, Multi-wavelength photoacoustic imaging of inducible tyrosinase reporter gene expression in xenograft tumors. *Sci. Rep.* **4** (5329), 1–7 (2014)
48. C. Qin, K. Cheng, K. Chen, X. Hu, Y. Liu, X. Lan, Y. Zhang, H. Liu, Y. Xu, L. Bu, X. Su, X. Zhu, S. Meng, Z. Cheng, Tyrosinase as a multifunctional reporter gene for photoacoustic/MRI/PET triple modality molecular imaging. *Sci. Rep.* **3**(1490), 1–8 (2013)
49. N.C. Deliollanis, A. Ale, S. Morscher, N.C. Burton, K. Schaefer, K. Radrich, D. Razansky, V. Ntziachristos, Deep-tissue reporter-gene imaging with fluorescence and optoacoustic tomography: a performance overview. *Mol. Imaging Biol.* **16**, 652–660 (2014)
50. J.F. Lovell, G. Zheng, Activatable smart probes for molecular optical imaging and therapy. *J. Innov. Opt. Health Sci.* **1**(1), 45–61 (2008)
51. J. Levi, S.R. Kothapalli, T.-J. Ma, K. Hartman, B.T. Khuri-Yakub, S.S. Gambhir, Design, synthesis, and imaging of an activatable photoacoustic probe. *J. Am. Chem. Soc.* **132**, 11264–11269 (2010)
52. J. Levi, S.R. Kothapalli, S. Bohndiek, J.-K. Yoon, A. Dragulescu-Andrasi, C. Nielsen, A. Tisma, S. Bodapati, G. Gowrishankar, X. Yan, C. Chan, D. Starcevic, S.S. Gambhir, Molecular photoacoustic imaging of follicular thyroid carcinoma. *Clin. Cancer Res.* **19**(6), 1494–1502 (2013)
53. K. Yang, L. Zhu, L. Nie, X. Sun, L. Cheng, C. Wu, G. Niu, X. Chen, Z. Liu, Visualization of protease activity in vivo using an activatable photo-acoustic imaging probe based on CuS nanoparticles. *Theranostics* **4**(2), 134–141 (2014)

54. A. Dragulescu-Andrasi, S.-R. Kothapalli, G.A. Tikhomirov, J. Rao, S.S. Gambhir, Activatable oligomerizable imaging agents for photoacoustic imaging of furin-like activity in living subjects. *J. Am. Chem. Soc.* **135**, 11015–11022 (2013)
55. D. Razansky, N.J. Harlaar, J.L. Hillebrands, A. Taruttis, E. Herzog, C.J. Zeebregts, G.M. van Dam, V. Ntziachristos, Multispectral optoacoustic tomography of matrix metalloproteinase activity in vulnerable human carotid plaques. *Mol. Imaging Biol.* **14**, 277–285 (2011)
56. Z. Zha, Z. Deng, Y. Li, C. Li, J. Wang, S. Wang, E. Qu, Z. Dai, Biocompatible polypyrrole nanoparticles as a novel organic photoacoustic contrast agent for deep tissue imaging. *Nanoscale* **5**, 4462–4467 (2013)
57. J. Liu, J. Geng, L.-D. Liao, N. Thakor, X. Gao, B. Liu, Conjugated polymer nanoparticles for photoacoustic vascular imaging. *Polymer Chem.* **5**, 2854–2862 (2014)
58. G. Balasundaram, C.J.H. Ho, K. Li, W. Driessen, U.S. Dinis, C.L. Wong, V. Ntziachristos, B. Liu, M. Olivo, Molecular photoacoustic imaging of breast cancer using an actively targeted conjugated polymer. *Int. J. Nanomed.* **10**, 387–397 (2015)
59. K. Pu, A.J. Shuhendler, J.V. Jokerst, J. Mei, S.S. Gambhir, Z. Bao, J. Rao, Semiconducting polymer nanoparticles as photoacoustic molecular imaging probes in living mice. *Nature Nanotech.* **9**, 233–239 (2014)
60. K.V. Kong, L.-D. Liao, Z. Lam, N.V. Thakor, W.K. Leong, M. Olivo, Organometallic carbonyl clusters: a new class of contrast agents for photoacoustic cerebral vascular imaging. *Chem. Comm.* **50**, 2601–2603 (2014)
61. S.K. Maji, S. Sreejith, J. Joseph, M. Lin, T. He, Y. Tong, H. Sun, S.W.-K. Yu, Y. Zhao, Upconversion nanoparticles as a contrast agent for photoacoustic imaging in live mice. *Adv. Mater.* doi:10.1002/adma.201400831 (2014)
62. U.S. Dinis, Z. Song, C.J.H. Ho, G. Balasundaram, A.B.E. Attia, X. Lu, B.Z. Tang, B. Liu, M. Olivo, Single molecule with dual function on nanogold: biofunctionalized construct for in vivo photoacoustic imaging and SERS biosensing. *Adv. Funct. Mater.* doi:10.1002/adfm.201404341 (2015)
63. S. Mallidi, G.P. Luke, S. Emelianov, Photoacoustic imaging in cancer detection, diagnosis, and treatment guidance. *Trends Biotechnol.* **29**(5), 213–221 (2011)
64. H.F. Zhang, K. Maslov, G. Stoica, L.V. Wang, Functional photoacoustic microscopy for high-resolution and noninvasive in vivo imaging. *Nature Biotechnol.* **24**, 848–851 (2006)
65. R.I. Siphanto, K.K. Thumma, R.G. Kolkman, T.G. van Leeuwen, F.F. de Mul, J.W. van Neck, L.N. van Adrichem, W. Steenbergen, Serial noninvasive photoacoustic imaging of neovascularization in tumor angiogenesis. *Opt. Express* **13**(1), 89–95 (2005)
66. J. Staley, P. Grogan, A.K. Samadi, H. Cui, M.S. Cohen, X. Yang, Growth of melanoma brain tumors monitored by photoacoustic microscopy. *J. Biomed. Opt.* **15**(4), 040510 (2010)
67. J.-T. Oh, M.-L. Li, H.F. Zhang, K. Maslov, Three-dimensional imaging of skin melanoma in vivo by dual-wavelength photoacoustic microscopy. *J. Biomed. Opt.* **11**(3), 034032 (2006)
68. G. Ku, X. Wang, X. Xie, G. Stoica, L.V. Wang, Imaging of tumor angiogenesis in rat brains in vivo by photoacoustic tomography. *Appl. Opt.* **44**(5), 770–775 (2005)
69. M.-L. Li, J.-T. Oh, X. Xie, G. Ku, W. Wang, C. Li, G. Lungu, G. Stoica, L.V. Wang, Simultaneous molecular and hypoxia imaging of brain tumors in vivo using spectroscopic photoacoustic tomography. *Proc. IEEE* **96**(3), 481–489 (2008)
70. D. Wu, L. Huang, M.S. Jiang, H. Jiang, Contrast agents for photoacoustic and thermoacoustic imaging—a review. *Int. J. Mol. Sci.* **15**(12), 23616–23639 (2014)
71. S.V. Hudson, J.S. Huang, W. Yin, S. Albeituni, J. Rush, A. Khanai, J. Yan, B.P. Ceresa, H.B. Frieboes, L.R. McNally, Targeted noninvasive imaging of EGFR-expressing orthotopic pancreatic cancer using multispectral optoacoustic tomography. *Cancer Res.* **74**(21), 6271–6279 (2014)
72. J.P. Mota, J.L.C. Carvalho, S.S. Carvalho, P.R. Barja, Photoacoustic technique applied to skin research: characterization of tissue, topically applied products and transdermal drug delivery. *Acoustic Waves—From Microdevices to Helioseismology (Intech)* (2011)

73. E.Z. Zhang, B. Povazay, J. Laufer, A. Alex, B. Hofer, B. Pedley, C. Glittenberg, B. Treeby, B. Cox, P. Beard, W. Drexler, Multimodal photoacoustic and optical coherence tomography scanner using an all optical detection scheme for 3D morphological skin imaging. *Biomed. Opt. Express* **2**(8), 2202–2215 (2011)
74. C. Kim, E.C. Cho, J. Chen, K.H. Song, L. Au, C. Favazza, Q. Zhang, C.M. Cobley, F. Gao, Y. Xia, L.V. Wang, In vivo molecular photoacoustic tomography of melanomas targeted by bioconjugated gold nanocages. *ACS Nano* **4**(8), 4559–4564 (2010)
75. X. Wang, Y. Pang, G. Ku, X. Xie, G. Stoica, L.V. Wang, Noninvasive laser-induced photoacoustic tomography for structural and functional in vivo imaging of the brain. *Nat. Biotechnol.* **21**(7), 803–806 (2003)
76. X. Wang, X. Xie, G. Ku, L.V. Wang, G. Stoica, Noninvasive imaging of hemoglobin concentration and oxygenation in the rat brain using high-resolution photoacoustic tomography. *J. Biomed. Opt.* **11**(2), 024015 (2006)
77. N.C. Burton, M. Patel, S. Morscher, W.H. Driessen, J. Claussen, N. Beziere, T. Jetzfellner, A. Taruttis, D. Razansky, B. Bednar, V. Ntziachristos, Multispectral opto-acoustic tomography (MSOT) of the brain and glioblastoma characterization. *NeuroImage* **65**, 522–528 (2013)
78. M.F. Kircher, A. de la Zerda, J.V. Jokerst, C.L. Zavaleta, P.J. Kempen, E. Mittra, K. Pitter, R. Huang, C. Campos, F. Habte, R. Sinclair, C.W. Brennan, I.K. Mellinshoff, E.C. Holland, S.S. Gambhir, A brain tumor molecular imaging strategy using a new triple-modality MRI-photoacoustic-Raman nanoparticle. *Nature Med.* **18**(5), 829–835 (2012)
79. S. Zackrisson, S.M. van de Ven, S.S. Gambhir, Light in and sound out: emerging translational strategies for photoacoustic imaging. *Cancer Res.* **74**(4), 979–1004 (2014)
80. A.D. Nunn, From clinical trials to prescriptions. *J. Nucl. Med.* **47**(12), 36N–37N (2006)
81. P.R. Crippa, C. Viappiani, Photoacoustic studies of non-radiative relaxation of excited states in melanin. *Eur. Biophys. J.* **17**(6), 299–305 (1990)
82. S.D. Nathanson, Insights into the mechanisms of lymph node metastasis. *Cancer* **98**(2), 413–423 (2003)
83. C. Kim, K.H. Song, F. Gao, L.V. Wang, Sentinel lymph nodes and lymphatic vessels: noninvasive dual-modality in vivo mapping by using indocyanine green in rats—volumetric spectroscopic photoacoustic imaging and planar fluorescence imaging. *Radiology* **255**(2), 442–450 (2010)
84. G.C. Langhout, D.J. Grootendorst, O.E. Nieweg, M.W.J.M. Wouters, J.A. van der Hage, J. Jose, H. van Boven, W. Steenbergen, S. Manohar, T.J.M. Ruers, Detection of melanoma metastases in resected human lymph nodes by noninvasive multispectral photoacoustic imaging. *Int. J. Biomed. Imaging* **163652**, 1–7 (2014)
85. S.A. Ermilov, T. Khamapirad, A. Conjusteau, M.H. Leonard, R. Lacewell, K. Mehta, T. Miller, A.A. Oraevsky, Laser photoacoustic imaging system for detection of breast cancer. *J. Biomed. Opt.* **14**(2), 024007 (2009)
86. Taruttis et al., Multispectral optoacoustic vascular imaging in the lower extremities: a comparison to clinical duplex ultrasound. Submitted (2015)
87. A. Dima, V. Ntziachristos, Non-invasive carotid imaging using optoacoustic tomography. *Opt. Express* **20**(22), 25044–25057 (2012)
88. Ford et al., Structural and functional analysis of intact hair follicles and pilosebaceous units by volumetric multispectral optoacoustic tomography. Submitted (2015)
89. T. Ida, Y. Kawaguchi, S. Kawachi, K. Iwaya, H. Tsuda, D. Saitoh, S. Sato, T. Iwai, Real time photoacoustic imaging system for burn diagnosis. *J. Biomed. Opt.* **19**(8), 086013 (2014)
90. J. Aguirre, M. Schwarz, D. Soliman, A. Buehler, M. Omar, V. Ntziachristos, Broadband mesoscopic optoacoustic tomography reveals skin layers. *Opt. Lett.* **39**(21), 6297–6300 (2014)
91. L. Vionnet, J. Gateau, M. Schwarz, A. Buehler, V. Ermolayev, V. Ntziachristos, 24-MHz scanner for optoacoustic imaging of skin and burn. *IEEE Trans. Med. Imaging* **33**(2), 535–545 (2014)
92. M. Omar, M. Schwarz, D. Soliman, P. Symvoulidis, V. Ntziachristos, Pushing the optical imaging limits of cancer with multi-frequency-band raster-scan optoacoustic mesoscopy (RSOM). *Neoplasia* **17**(2), 208–214 (2015)

93. N. Bézière, C. von Schacky, Y. Kosanke, M. Kimm, A. Nunes, K. Licha, M. Aichler, A. Walch, E.J. Rummeny, V. Ntziachristos, R. Meier, Optoacoustic imaging and staging of inflammation in a murine model of arthritis. *Arthritis Rheumatol.* **66**(8), 2071–2078 (2014)
94. C. Lutzweiler, R. Meier, E. Rummeny, V. Ntziachristos, D. Razansky, Real-time optoacoustic tomography of indocyanine green perfusion and oxygenation parameters in human finger vasculature. *Opt. Lett.* **39**(14), 4061–4064 (2014)